RSC Advances

PAPER

View Article Online
View Journal | View Issue

Cite this: *RSC Adv.*, 2021, **11**, 32408

3D-printed monolithic biofilters based on a polylactic acid (PLA) – hydroxyapatite (HAp) composite for heavy metal removal from an aqueous medium†

Natalia Fijoł,[a] Hani Nasser Abdelhamid,[ab] Binsi Pillai,[c] Stephen A. Hall,[de] Nebu Thomas[f] and Aji P. Mathew *[a]

Received 6th July 2021
Accepted 23rd September 2021

DOI: 10.1039/d1ra05202k

rsc.li/rsc-advances

High flux, monolithic water purification filters based on polylactic acid (PLA) functionalised with fish scale extracted hydroxyapatite (HAp) were prepared by solvent-assisted blending and thermally induced phase separation (TIPS), followed by twin-screw extrusion into filaments and processed *via* three-dimensional (3D) printing. The printed filters with consistent pore geometry and channel interconnectivity as well as homogenous distribution of HAp in the PLA matrix showed adsorption capabilities towards heavy metals *i.e.* cadmium (Cd) and lead (Pb) with maximum adsorption capacity of 112.1 mg g_{HAp}^{-1} and 360.5 mg g_{HAp}^{-1} for the metal salt of Pb and Cd, respectively. The adsorption was found to be driven by a combination of ion exchange, dissolution and precipitation on HAp and surface complexation.

1. Introduction

The demand for clean drinking water has been increased by a factor of six over the past decade due to the industrial revolution and growing population.[1] According to the United Nations report for water development,[1] the global population used 68–91% of improved drinking water source and sanitation facilities. The report also observed that 80% of wastewater was discharged without proper treatment. Water contamination with heavy metals such as cadmium (Cd) or lead (Pb) is one of the primary sources of hazardous pollutants causing several health problems for human beings, animals, and plants.[2,3] Removal of heavy metals can be achieved *via* several methods such as chemical precipitation, oxidation/reduction, ion-exchange, filtration, sedimentation, adsorption, reverse osmosis, and electrochemical treatment.[4,5]

Adsorption is the widely applicable method for water treatment due to its simple procedure and capability to treat larger volumes of contaminated water. Natural materials such as cellulose[6,7] and chitin,[8] and hydroxyapatite (HAp)-based materials have been intensively used as adsorbents to remove heavy metals.[9,10] Hydroxyapatite (HAp), with the general formula $Ca_{10}(PO_4)_6(OH)_2$, is the primary mineral component of bone and teeth. It is used extensively in medical applications as bone regeneration scaffolds or biocompatible coatings,[11–13] in the pharmaceutical and chemical industry for separation,[14] and in the environmental remediation industry to purify the air, water and soil.[15] Two distinct binding sites in HAp namely C and P sites are key in using HAp in environmental treatment; positively charged C sites containing calcium ions that can absorb anionic species and negatively charged P sites with phosphate groups that can adsorb cationic species such as metal ions.

The hydroxyapatite (HAp) crystals or nanoscale hydroxyapatite (nHAp) crystals are usually synthesized by solid-state reactions, crystal growth under hydrothermal reaction, layer hydrolysis of other calcium phosphate salts and sol–gel crystallization .[12,13] The HAp crystals can also be isolated from biological sources such as mineral rocks, plants, and more importantly from biological waste such as animal bones (fish, chicken and bovine bones), and biogenic products (eggshells, molluscan shells, corals).[16] Due to the low production cost and the worldwide availability, the use of fish scale bio-waste for the processing of HAp crystal has gained momentum[17,18] and found

[a]*Department of Materials and Environmental Chemistry, Stockholm University, Frescativägen 8, 106 91, Stockholm, Sweden. E-mail: aji.mathew@mmk.su.se; Tel: +46 8161256*

[b]*Advanced Multifunctional Materials Laboratory, Department of Chemistry, Faculty of Science, Assiut University, Assiut 71515, Egypt*

[c]*ICAR-Central Institute of Fisheries Technology, Matsyapuri, Willington Island, Cochin, India – 682 029*

[d]*Division of Solid Mechanics, Lund University, Lund, Sweden*

[e]*Lund Institute of Advanced Neutron and X-Ray Science, Lund, Sweden*

[f]*Department of Periodontology, Pushpagiri College of Dental Sciences, Thiruvalla, Kerala, India*

† Electronic supplementary information (ESI) available: (S1) disc shaped printed structures used for adsorption study and the SEM images, (S2) TGA curves of 3D printed filaments (S3) elemental composition using XPS data, (S4) characterization of Pb adsorbed into HAp/PLA (S5) characterization of Pb adsorbed into HAp/PLA are given. The 3D printed water treatment prototypes, thermal stability data, XPS data, μ-CT measurement video. See DOI: 10.1039/d1ra05202k

application as a bioactive component in the biomedical field.[19] It is, however, known for its inferior mechanical properties.[20] Moreover, utilization of HAp or nHAp in powder form is limited and calls for suitable material processing to meet the targeted application requirements. In the case of water treatment, it is essential to develop products that combine versatile surface chemistry, adsorption capacity with high water flux and mechanical and dimensional stability in moist environment. Literature shows that HAp composites with poly(lactic acid),[10] polyacrylamide,[21] polyurethane,[22] magnetic nanoparticles (Fe_3O_4/HAp)[23,24] and magnetic nanoparticles–immobilized oxidized multiwall carbon nanotubes (mHAP–oMWCNTs)[25] in the form of powder, hydrogels and foams were used in water treatment.

In this context, 3D printing offers a possibility to develop monolithic HAp composite filters, with charge–specific adsorption capability, tuned pore structure, interconnected pores and easy handling during water treatment. Therefore, a PLA-based composite reinforced with fishbone extracted HAp was prepared in the current work, which contributes to resource recovery and resource efficient environmental remediation concept. Polylactic acid (PLA) is chosen as the matrix phase due to its biobased origin and biodegradability and the well-established 3D printability and the flexibility of the biocomposites processing. Combining the 3D printing of PLA and PLA-based composites for water treatment applications is a relatively new concept, however there has been several studies showing the potential of PLA and PLA-based compounds for oil and water separation[26–28] as well as heavy metal[29] and volatile organic compounds[30] removal from water. The role of PLA as the matrix phase is to bind the filler particles together, while also providing separation between individual particles or particle clusters in order to control crack formation and propagation throughout the filter's structure. Moreover, PLA provides rigidity and shape of the overall filter structure. In terms of processing by the means of 3D printing, PLA provides the structure with a high surface finish.

Thermally Induced Phase Separation (TIPS) method gained scientific interest as it has been shown to improve the dispersion of hydrophilic nanofillers in the hydrophobic matrix, which could enhance the material's final properties and the ease of its processing.[31,32] The preparation of PLA/HAp[33] and HAp/poly(methyl methacrylate) (PMMA)[34] composites *via* TIPS method was shown to result in a hybrid system with a potential application in the biomedical field. Within this study, PLA/HAp biocomposite pellets were prepared by the (TIPS) method. Upon completion of the TIPS procedure, the obtained biocomposite pellets were twin-screw extruded into 3D printing filaments, which were further successfully utilized within the fused deposition modelling (FDM) process.

The processing of PLA-based composites by additive manufacturing, also called 3-dimensional (3D) printing and more specifically by Fused Deposition Modelling (FDM), offers various advantages compared to traditional processing methods such as casting and injection moulding. Firstly, 3D printing does not require expensive tools and it is generally cost and time effective technique. Moreover, it gives a possibility to produce complex models with very well-controlled geometries and pore structure, while generating low material losses and low environmental impact.[35–37] The reinforcement of PLA polymer with various fillers such as hemp,[38] cellulose[39] and bamboo[40] fibers to improve the polymer's mechanical and thermal properties is a popular approach in the last years. Several PLA-based composites reinforced with various nature-derived fillers such as wood flour,[41] microcellulose[42] and carbon fibers[43,44] were successfully 3D printed with the use of the FDM technique. The hydroxyapatite (HAp)/PLA based composites designated for promoting bone growth were previously developed and successfully 3D-printed into scaffolds,[17,45–48] however to the best of the authors' knowledge the utilization of the TIPS method for the preparation of such 3D-printable composites combined with their potential application within the water treatment industry has not yet been reported.

In this study, the prototypes in the form of 20 × 20 × 20 mm cubes with both gradient and uniform porosity structure and the porous disc-shaped models with a diameter of 6 mm, were designed to meet multifunctional requirements and find application in water treatment. This study is expected to provide a viable and scalable route to use low-cost and readily available biobased resources to produce filters for environmental remediation. The chemistry, morphology, water permeance performance of the 3D structure and adsorption of metal ions on HAp particles incorporated into the 3D printed filters is reported.

2. Experimental

2.1 Materials and methods

The raw materials used for the preparation of the 3D printable biocomposite included transparent polylactic acid (PLA) pellets (Ingeo™ Biopolymer 4043D, Nature Works, provided by Add North 3D AB, Sweden), 1,4-dioxane (anhydrous, 99,8%, Carlo Erba Reagents, Spain) and hydroxyapatite (HAp) powder.

The chemicals used within the adsorption studies included: lead nitrate ($Pb(NO_3)_2$, 98%) and cadmium nitrate ($Cd(NO_3)_2$) purchased from Sigma-Aldrich (Germany).

2.1.1. HAp extraction procedure. The HAp was extracted using a standardised laboratory protocol. Briefly, fish scales were collected from fresh water fish (*Catla catla*) and the extraneous matter and pigments were removed by scrubbing and repeated washing in running tap water. The cleaned scales were initially deproteinized by hydrolysis using enzyme alkalase (0.5% of the protein content of scale (w/w) for 6 h at 55 °C). The decollagenised scales were separated by filtration and dried at 100 °C in a hot air oven for 6 hours. Further, the dried fish scales were sintered at 450 °C for 2 h followed by the second stage of sintering at 900 °C for different durations of 3 h to yield a fine powder of HAp. The HAp powder thus obtained was stored in airtight container at ambient temperature.

2.1.2. Preparation of PLA/HAp composite pellets by thermally induced phase separation (TIPS) route. The 10% PLA solution was prepared by dissolving PLA pellets in 1,4-dioxane by overnight magnetic stirring at room temperature. The hydroxyapatite (HAp) powder was then added to the solution

and stirred for 2 h. The obtained 15% PLA/HAp solution was then added dropwise into liquid nitrogen to form composite pellets. The pellets were further freeze-dried for 48 h and Add North 3D AB, Sweden, extruded the final, freeze-dried product into printable filaments.

2.1.3. 3D printing. All of the porous filters were designed based on a simple cubic and cylindrical CAD models. The dimensions and the porosity of the structures were adjusted using the CURA slicing software prior to generating the G-code file necessary for being processed by the printer. The printers used within the study were Ultimaker S5 (for printing out the reference PLA prototypes) and Ultimaker 2+ (for printing out the PLA/HAp biocomposite) from Ultimaker BV, The Netherlands. The printing parameters used for both filaments were as follows; nozzle diameter: 400 μ, layer thickness: 150 μ and bed temperature: 90 °C. The nozzle temperature was set to 210 °C and 230 °C for the PLA filament and PLA/HAp filament, respectively. The print speed was set to 40 mm s^{-1} and 50 mm s^{-1} for the PLA (reference) and PLA/HAp filament, respectively. The printed monolithic filters were used for further characterization.

Different structures were printed using PLA and PLA/HAp biocomposite 3D printing filaments. The printing parameters were optimised for each structure as summarised below:

The printing parameters for discs with radius of 6 mm and thickness of 3 mm were: infill density: 75%, infill line distance: 0.5 mm, printing speed: 30 mm s^{-1}. The discs were used for heavy metal adsorption study (see the photographs and the SEM images in Fig. S1†).

The printing parameters for the 20 × 20 × 20 mm gradient porosity cube were: infill density: 40%, infill line distance: 0.8 mm, gradual infill steps: 2, gradual infill height: 7 mm, print speed: 45 mm s^{-1}. The 20 × 20 × 20 mm uniform porosity cube's printing parameters were: infill density: 40%, infill line distance: 0.8 mm, print speed: 45 mm s^{-1}.

2.2 Characterization of the PLA/HAp biocomposite

2.2.1. Transmission electron microscopy (TEM). The detailed morphology and microstructure of the HAp starting powder was examined by JEOL-JEM 2100F transmission electron microscope (TEM) equipped with a Gatan UltraScan CCD. The accelerating voltage used was 200 kV. High-resolution transmission electron microscopy (HRTEM) images of crystals were obtained using the same equipment.

2.2.2. Scanning electron microscopy (SEM). The morphology and composition of biocomposite pellets as well as the pore structure and composition of the 3D printed porous filters, were tested with the use of Hitachi TM3000, Tabletop Microscope (Hitachi Ltd, Japan) and JEOL JSM-7000F Analytical Scanning Electron Microscope (JEOL Ltd, Japan). The samples were tested in relatively low accelerating voltage (in the range between 2–15 kV) in both secondary electron and back-scattered electron (TOPO and COMPO) mode. The elemental composition of the biocomposite was assessed. All the samples were prepared for the microscopic examination by sputtering them with a thin layer of gold (in the cycle of 60 seconds from the distance of 7 cm).

2.2.3. Fourier-transform infrared spectroscopy (FTIR). The PLA pellets as well as the developed PLA/HAp biocomposite were analyzed by infrared spectroscopy with Varian 610-IR FT-IR spectrometer (Varian Inc., CA, USA) equipped with the Specac Golden Gate single reflection attenuated total reflection (ATR) accessory with a diamond ATR element (Specac, UK) for quick measurements. Sixteen scans between 4000 cm^{-1} and 400 cm^{-1} were averaged for each spectrum at intervals of 1 cm^{-1} with a resolution of 4 cm^{-1}.

2.2.4. Powder X-ray diffraction (PXRD). To collect the samples' fingerprint and assess the crystallinity of the developed biocomposite, PXRD was performed. The data was collected on a PANalytical X'Pert PRO MRD City (Malvern Instruments, UK) with copper radiation (λ = 1.54056 Å) with a scan range between 5° and 40°. The PXRD measurements were collected for the starting materials *i.e.* PLA pellets and HAp powder, as well as for the developed PLA/HAp biocomposite in the form of freeze-dried pellet.

2.2.5. Thermogravimetric analysis (TGA). The thermal decomposition of the PLA/HAp composite in the form of freeze-dried pellets, custom extruded biocomposite filament and PLA/HAp composite print as well as the reference PLA samples, were analysed with the use of STA 449 F1 Jupiter (Netzsch Instruments, Germany). 10–20 mg of samples were placed in ceramic cups and heated from 30 °C up to 1350 °C at a heating rate of 10 °C min^{-1} under an air flow of 40 mL min^{-1}.

2.3 Characterization of the 3D printed biofilters

2.3.1. X-ray micro-computed tomography (μCT). The pore structure and the dispersion of the HAp filler in the PLA matrix in the uniform and gradient cubes were evaluated with the use of a 3D X-ray microscope (Zeiss Xradia Versa XRM520). The tomographic data acquisition involved 1601 projections of 1024 × 1024 pixels, acquired over 360° sample rotation with the X-ray source set to 60 kV and 5 W. Two data sets were acquired with different sample-to-detector distances and reconstructed, with the Zeiss Reconstructor software, to yield 3D image volumes with cubic voxels of widths 24 μm and 8 μm. The acquisition used 1 s and 1.7 s exposure time per image, respectively. The 24 μm images covered the full sample diameter and the 8 μm images covered an internal cylindrical field of view of about 8 mm diameter.

2.3.2. Permeability and flux measurements. The water permeance through the 3D printed biofilters was measured by filtering deionized water using an in-house-constructed water permeance instrument in the dead-end filtration mode. The measurements were conducted at room temperature and water temperature of 20 °C at a constant flow of 1500 cm^3 min^{-1}. The flux performance of the samples was measured at constant pressure (p) by calculating the exact time (t) needed for 2 L of water (V) to pass through the filter with the cross-sectional area (A) (eqn (1)).

The permeability (k) values were calculated based on Darcy's equation (eqn (2)), where μ is water viscosity, A is the filter's

cross-sectional area, q is the measured fluid flow rate, l is filter's height and Δp is the difference between measured inlet and outlet pressure.

$$\text{Flux} = \frac{V}{t \times A \times p} \quad (1)$$

$$k = -\frac{\mu q}{A\frac{\Delta p}{l}} \quad (2)$$

2.3.3. Adsorption study. Adsorption experiments were carried out by adding 3D printed circular disk (6 mm × 3 mm, average weight 0.314 g, 15 wt% HAp) to 100 mL of $Pb(NO_3)_2$ or $Cd(NO_3)_2$ solutions at a given concentration (5 mg, 10 mg, 50 mg, and 100 mg). The suspensions were stirred at a constant speed of 500 rpm for 12 h. The concentration of Cd^{2+} and Pb^{2+} in the supernatant was determined using inductively coupled plasma atomic emission spectroscopy (ICP-OES, Thermo Scientific iCAP 6200). The adsorption capacity (q, mg g^{-1}), and adsorption efficiency (%) were calculated as follows:

$$\text{Adsorption capacity } (q,\ \text{mg g}^{-1}) = \frac{(C_0 - C_e)}{m} \quad (3)$$

$$\text{Adsorption efficiency } (\%) = \frac{C_0 - C_e}{C_0} \times 100 \quad (4)$$

where C_0 and C_e (mg) are the initial and equilibrium concentration in aqueous solution, respectively, and m (g) is the mass of HAp adsorbents.

Selectivity of adsorption toward metals was measured *via* soaking 3D objects in a solution (300 mL) of metal ions ($Co(NO_3)_2$, $Cu(NO_3)_2$, $Pb(NO_3)_2$, $Cd(NO_3)_2$, $Zn(NO_3)_2$, $AlCl_3$, and $FeCl_3$, 50 ppm for each element). The adsorbent was soaked for 12 h before analysis using EDX analysis. Selectivity was calculated using the following equation:

$$\text{Selectivity } (\%) = \frac{[\text{Metal concentration, wt\%}]}{[\text{Total metal concentration, wt\%}]} \times 100 \quad (5)$$

2.3.4. X-ray photoelectron spectroscopy (XPS). XPS analysis for 3D printing objects after adsorption of Cd and Pb was done using Thermo Fischer (K-alpha, monochromated, Al Kα radiation, 1486.6 eV). XPS for 3D PLA was performed on the same object after soaking in a solution of NH_4F to remove HAp.

3. Results and discussion

3.1. Preparation of the hydroxyapatite (HAp)/polylactic acid (PLA) biocomposite

Dispersing HAp in the PLA matrix was a crucial step in the processing of the 3D printable biocomposite filaments. Solvent-assisted blending and subsequent thermally induced phase separation (TIPS) method was used for the preparation of spherical pellets of polylactic acid (PLA) composites reinforced with the fish scale extracted hydroxyapatite (HAp) (Fig. 1). The obtained pellets were suitable for melt extrusion into 3D printing filaments. The uniform and gradient porous cubic filters were successfully developed (Fig. 1). The most commonly reported 3D printable PLA-HAp composites are prepared by direct extrusion-compounding.[45,46,49,50] The TIPS method could be an efficient alternative as a tuneable process that can enhance the filler dispersion *via* the development of a well-interconnected polymer network.[51] In the current study, due to the significant roughness of the biocomposite 3D printing filament, the printability of the PLA/HAp system was initially challenging, however with optimization of the printing parameters the challenge was overcome.

The TGA curves of the PLA and PLA/HAp 3D printing filaments are given in Fig. S2.† The PLA had the onset degradation temperature T_x of 297 °C and around 400 °C the PLA sample decomposed almost completely, which correlates with previous reports.[52] PLA/HAp composite filaments indicated a residual weight of 15.4 wt% above 415 °C where the PLA is fully decomposed, confirming a 15 wt% loading of HAp in the composite. The residual weight in the composite remained stable at 15% until <1000 °C.

3.2. Structural characterisation of biocomposite and 3D printed filter

The transmission electron microscopy (TEM) analysis of the HAp powder revealed irregular particles with a size of 50–200 nm (Fig. 2a). A high-resolution TEM (HR-TEM) image proves the crystalline character of HAp with a lattice plane of 0.28 nm corresponding to Miller index (211) (Fig. 2b). The corresponding Fast Fourier Transform (FFT) image shows strong diffraction spots indicating the powder's high crystallinity (Fig. 2c). The SEM images of the HAp powder (Fig. 2d) revealed that the particle size distribution is not entirely homogenous, and there are clusters and agglomerates present in the powder. The average particle diameter measured with the Image J software showed an average diameter around 46 μm. During different stages of the processing the HAp morphology and dispersion in PLA phase were monitored. Fig. 2e shows that HAp particles are dispersed in the PLA matrix after completion of the TIPS process and the freeze-drying procedure. It was noted that the particle diameter significantly decreased to an average of 16 μm, but the overall homogeneity of the biocomposite was not satisfactory as big clusters can still be observed in the surface and the cross-section images. The HAp dispersion in the PLA matrix gets significantly improved after the extrusion process into the 3D printing filament as shown in Fig. 2f. Regardless of the presence of HAp clusters and agglomerates, the overall distribution of the HAp filler in the matrix within the filament is more homogenous than in the case of the freeze-dried pellet itself. Moreover, the average HAp particle diameter further decreased to around 11 μm in the filaments. Therefore, a gradual improvement in the distribution and dispersion of HAp particles in the PLA matrix was achieved during the processing, however the particle sizes did not reach the nanometre scale.

The pore and channel structure as well as the distribution of functional HAp in the matrix of the 3D printed biofilters were

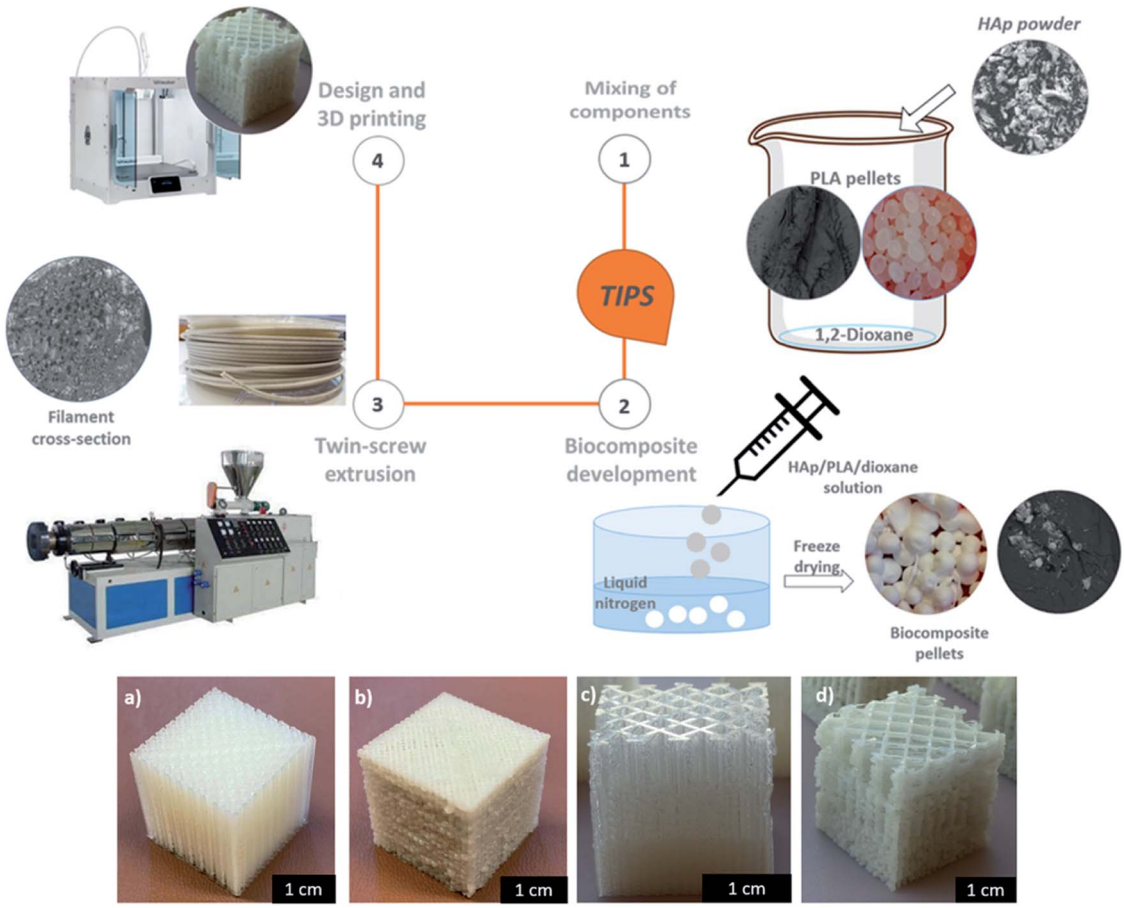

Fig. 1 Overview of biocomposite 3D printing process and the printed prototypes: (a) uniformly porous reference PLA filter, (b) corresponding PLA/HAp filter, (c) gradient porosity reference PLA filter, (d) corresponding PLA/HAp filter.

examined using SEM. Fig. 2g and h shows the pore structure of the uniform (a) and gradient (b) porous cubic filters. Notably, the channel interconnectivity was maintained throughout the entire filter structure in both cases, confirming its potential applicability in water purification with direct water flux. The average pore size of the uniform cube was 572 ± 33 μm (measured using Image J from obtained SEM images), which differs from the programmed pore size of 800 μm indicating the shrinkage of the PLA/HAp biocomposite during the 3D printing procedure. The average pore size for the gradient cube was measured individually for each gradient-step cross-section. The pore sizes ranged from 463 ± 40 μm, through 1.3 ± 0.2 mm up to 3.2 ± 0.5 mm. The programmed pore sizes were 800 μm, 1.6 mm and 3.2 mm, showing that especially for the smaller pores there was a significant shrinkage of the material during the printing process. Regardless of the fact that final pore sizes differ from the programmed ones, it is observable that both the size and geometry of the pores were consistent for the uniform and gradient filter models, proving good printability of the composite.

Moreover, the micro-morphological features of the 3D printed PLA/HAp biocomposite filters with uniform porosity structure were assessed with the use of μCT. It can be observed (Fig. 2i) that the HAp filler within the PLA matrix is homogeneously distributed throughout the entire structure of the filter. The cross-section images (Fig. 2j–l) present the dispersion and distribution of the HAp in the PLA in the inner walls of the biofilter. Overall, both the dispersion and distribution are consistent and homogenous both in the outer walls and around the pores. See video file (PLA-HAp_CubeUnif_3Dmovie.mpg) showing the 3D structure of filter in the ESI.† This indicates the applicability of biofilters for contaminant adsorption under the direct flux of water, as the HAp sites seem to be very accessible for interaction with metal ions. Moreover, the cross-section images (Fig. 2j–l) provide information on the print quality. There are a few micro-interruptions in the printed pattern, which are not observable with a naked eye. The print pattern interruptions were most likely introduced during slight clogging of the filament during the FDM process. The clogging was associated with the roughness of the PLA/HAp biocomposite filament, which translated onto the surface roughness of the printed biofilter, which can be of benefit for the application of choice. It is important to stress that the filter was designed without the thick outer shell, so that the porosity structure could be better assessed through the side walls.

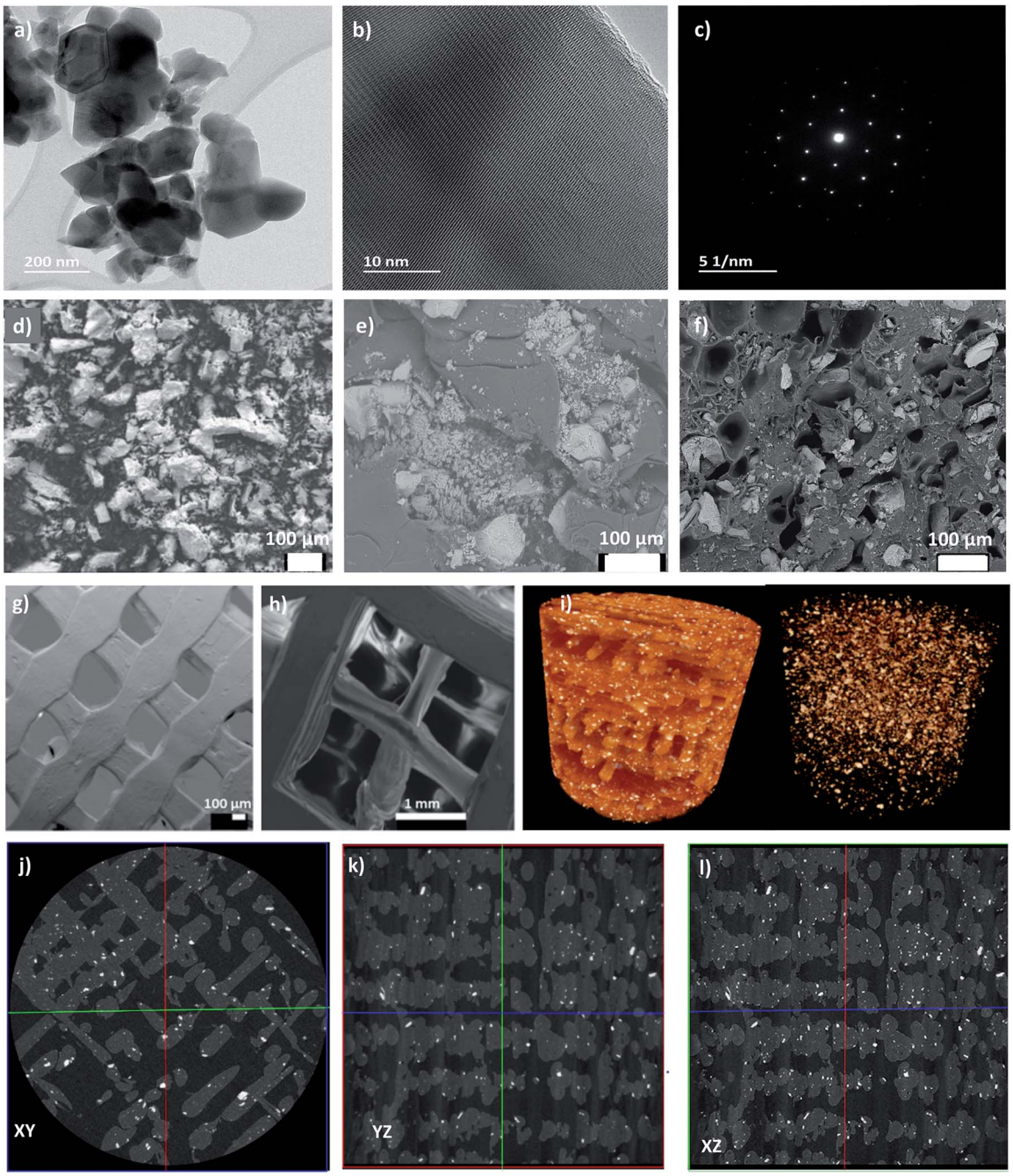

Fig. 2 (a) TEM micrograph showing the HAp powder particles, (b) HR-TEM image of the single powder particle, (c) FFT of the HAp single powder particle, (d) SEM image of HAp powder; (e) SEM image of PLA/HAp biocomposite pellet; (f) SEM image of the PLA/HAp filament cross-section, (g) porosity structure of the uniformly porous cube; (h) porosity structure of the gradient porous cube; (i) 3D rendering of the 8 µm µCT volume plus a rendering showing just the HAp in the biofilter; (j–l) µCT representative cross-sections of the 3D printed biofilters showing the dispersion of HAp in the PLA.

3.3 Chemical and crystalline structure of the biocomposite

Different functional groups in the biocomposite system were assessed using the Fourier transform infrared spectroscopy (FT-IR). The comparison between the starting materials, *i.e.* PLA pellet and HAp powder and the developed PLA/HAp biocomposite is presented in Fig. 3a. HAp powder with the stoichiometric chemical formula $Ca_{10}(PO_4)_6(OH)_2$ exhibited adsorption peaks characteristic of the natural HAp minerals. The intense peaks at 518 cm^{-1} and 1012 cm^{-1} are assigned to the PO_4^{3-} groups.[53] Spectral bands observable in the region between 900 cm^{-1} and 1200 cm^{-1} arise mainly from the symmetric and antisymmetric P–O stretching vibrations, whereas the bands detectable in the region between 500 cm^{-1} and 700 cm^{-1} correspond to the antisymmetric P–O bending

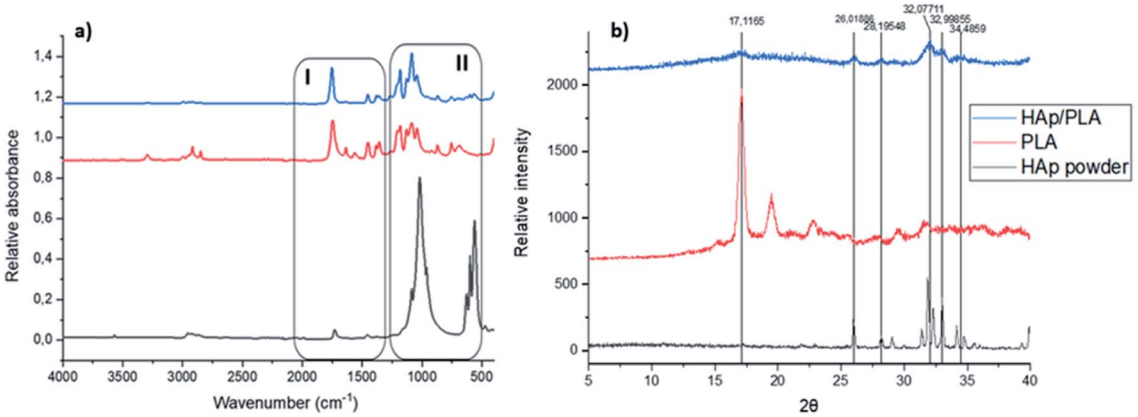

Fig. 3 (a) FT-IR spectra of the starting materials and PLA/HAp, (b) PXR diffraction patterns of the starting materials and PLA/HAp.

vibrations of the phosphate groups. The fact that the contour of the small band observable at 960 cm^{-1} is quite sharp and narrow indicates that the analysed HAp is of high crystalline.[54] The bands visible at 624 cm^{-1} and 3560 cm^{-1} are associated with vibrational and stretching vibrations of the OH– groups. As it comes to the spectral feature observable at 2952 cm^{-1}, it corresponds to the stretching vibrations of the (P–)O–H groups. The band at 1457 cm^{-1} and 1725 cm^{-1} to CO_3^{2-} and carbonyl groups, respectively.

FTIR spectra of pristine PLA, shows absorbance regions characteristic of the polyesters with ester functional groups, *i.e.* C=O and C–O groups. The bands observed at 1085 cm^{-1} and 1187 cm^{-1} correspond to C–O stretching vibrations, whereas the C=O stretching vibrations are associated with the bands observed at 1633 cm^{-1} and 1750 cm^{-1}. The spectral features observable at 1347 cm^{-1}, 1442 cm^{-1} and 1565 cm^{-1} correspond to C–H bending vibrations, and the C–H stretching vibrations are associated with the band observable at 2911 cm^{-1}.

In the PLA/HAp composite system, all the absorbance peaks corresponding to the starting materials (marked as region I and II) remained unaltered indicating a physical mixing of the two phases. The peaks observable at 566 cm^{-1}, 600 cm^{-1} and 630 cm^{-1} correspond to the phosphate groups' P–O bending vibrations of phosphate groups. The sharp peak observed at 1750 cm^{-1} corresponds to the stretching vibration of the carbonyl group and the peaks observable between 1350 and 1450 cm^{-1} correspond to the C–H bending vibrations. The C–O stretching vibrations are also observable at the biocomposite spectrum at precisely the same frequencies as the bands observable on the spectrum of the reference PLA.

The crystallinity data of the two starting materials, *i.e.* HAp powder and PLA pellets as well as for the freeze-dried PLA/HAp biocomposite pellet is shown in Fig. 3b also confirm the physical mixing of the two phases. Pristine PLA pellets exhibit a crystal structure with a sharp crystalline peak at 17.12° and in the PLA/HAp system, crystallinity peak at $2\theta = 17.12°$ was observable, however with a slightly lower intensity. Likewise, peaks corresponding to HAp crystal structure ($2\theta = 26.0°$; 28.2°; 32.1° and 32.1° and 34.5°) were observed for PLA/HAp composite.

3.4. Water flux and heavy metal adsorption

The flux and permeability measurements showed high-throughput character of the 3D printed filters. The flux measured was 1 777 275 ± 99 546 and 1 995 420 ± 34 484 (L m^{-2} h^{-1} bar^{-1}) for the uniform and gradient porosity cubic structures, respectively. No pressure was applied on the feed side during the measurement, which shows the potential of the 3D printed PLA/HAp composites as high water flux filters without the need for external pressure source and use of the electrical energy.

The set design porosity of the filter was approximately 40% and calculated permeability of the uniform and gradient cubic filters was 3.58×10^{-10} m^2 and 4.77×10^{-10} m^2, respectively. The calculated values are in the same range with values previously reported in the literature for the porous 3D printed models.[55,56]

The adsorption performance for 3D printing PLA/HAp was evaluated using Pb and Cd ions (Fig. 4). The adsorption capacity increased for Pb and Cd with the initial concentration of metal solution (Fig. 4a). The maximum adsorption efficiency was 45% and 40% for Cd and Pb, respectively, which decreased with the increase in initial metal concentration (Fig. 4b). The conclusions were drawn from the synthetic polluted water sample under controlled laboratory conditions, therefore further experiments are needed to establish whether the same results could be obtained using an actual wastewater sample from the industrial effluents. This is, however, not included within the scope of this work. PLA/HAp showed a maximum adsorption capacity of 360.5 mg g_{HAp}^{-1} and 112.6 mg g_{HAp}^{-1} for Cd, and Pb, respectively (Fig. 4b). The ionic radii has previously been reported as a factor influencing the heavy metal ions' adsorption efficiency onto various adsorbents.[57] Generally, the smaller the ion the better adsorption efficiency. The ionic radius of Cd^{2+} is 0.97 Å and that of Pb^{2+} is 1.20 Å, which could be one explanation for the higher adsorption capacity of Cd^{2+} ions when compared to Pb^{2+} ions. The adsorption of heavy metal on HAp can be achieved *via* ion-exchange, surface complexation, chelation to surface-modified molecules, dissolution of HAp and precipitation of metal phosphates, and the substitution of Ca in HAp by

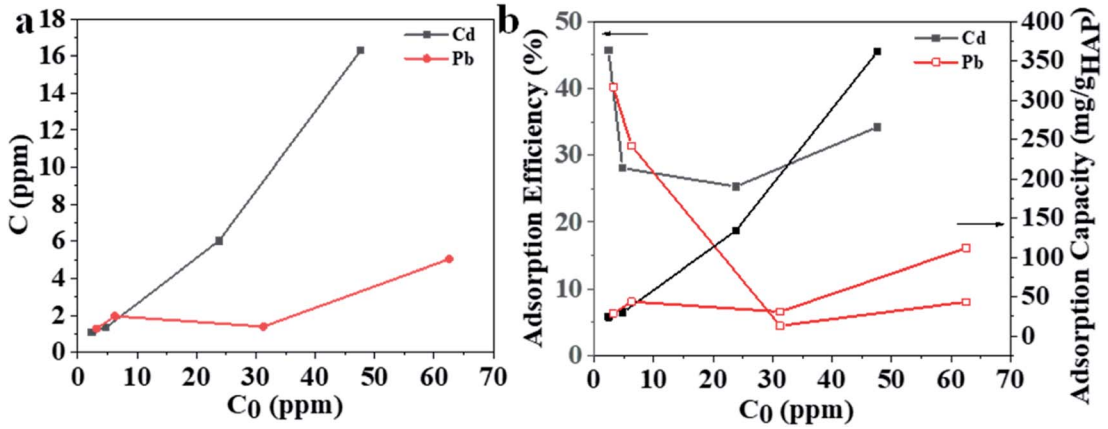

Fig. 4 (a) Adsorbed amount *versus* initial metal concentration and (b) adsorption efficiency/adsorption capacity *versus* initial metal concentration showing the water treatment potential of the 3D printed biocomposite filters.

the adsorbed metals during coprecipitation.[58] The interaction of Pb and HAp includes the dissolution of the hydroxyapatite, followed by the precipitation of lead hydroxyapatite.[58] The adsorption of Pb using magnetic nanoparticles/hydroxyapatite (Fe_3O_4/HAp) was proposed to take place *via* dissolution/precipitation and the surface complexation.[23] Cd adsorption using HAp might be achieved *via* a two-step mechanism; (1) rapid surface complexation *via* partial dissolution of hydroxyapatite and (2) ion exchange with Ca.[9,59–61] Different mechanisms of adsorption between the two different studied ions, could impact the adsorption capacity and efficiency. The Cd^{2+} ions were adsorbed by a two-step surface complexation mechanism, whereas Pb^{2+} by coprecipitation potentially indicating complexation being a more efficient and preferable method for heavy metal ion adsorption at high capacity.

The previous literature reports on the adsorption of Cd^{2+} and Pb^{2+} onto the hydroxyapatite structure *via* diverse, aforementioned mechanisms[9,23,58,62] together with the fact that both of the heavy metal ions in question are one of the most common contaminants in both the wastewater from industrial effluents[63–66] and freshwater reservoirs[67–69] makes them ideal candidates for investigation within this study. The adsorption mechanism of heavy metal ions onto the HAp/PLA structure was investigated using XPS (Fig. 5 and S3†), the SEM, and EDX analysis (Fig. S4 and S5†). After adsorption, the 3D printing of PLA/HAp materials shows the same elements, Ca_2P_3, and heavy metals Pb and Cd (Fig. 5a). The peaks at a binding energy of 531.3 eV and 531.1 eV were observed after adsorption of Cd and Pb, respectively, corresponding to Cd–O and Pb–O bonds (Fig. 5b). XPS data analysis indicates no change in the adsorbed Cd's oxidation state (Fig. 5c) and Pb species (Fig. 5d). After adsorption, SEM image and EDX mapping show coprecipitation of the adsorbed metals into the 3D printing objects with HAp (Fig. S4 and S5†). The possibility of entrapment of Cd^{2+} and Pb^{2+} ions within the filter pores was investigated with the use of EDX mapping, which clearly showed binding of the heavy metal ions onto the filter's walls, while leaving the pores empty and unaffected (Fig. S4c†). These observations, combined with the XPS results strongly indicate chemical nature of bonding between the filter's structure and both of the heavy metal ions.

Selectivity for metal adsorption has been tested for a water solution containing mixed metal ions (Fig. 6). The adsorption was tested for pristine 3D objects and the hybrid adsorbent (denoted as Pb@PLA/HAp and Cd@PLA/HAp for Pb and Cd, respectively) that were used for the adsorption. Pb@PLA/HAp

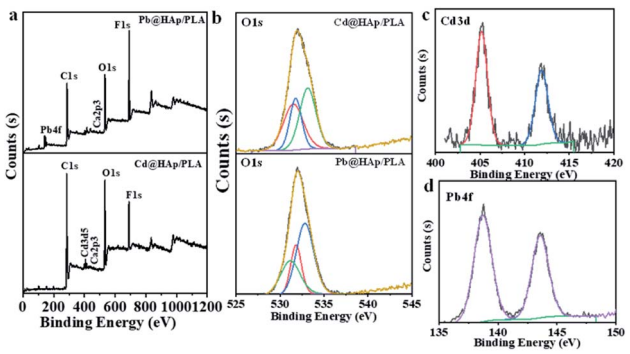

Fig. 5 XPS analysis of 3D printed PLA and 3D printed PLA/HAp after adsorption of Pb^{2+} and Cd^{2+}, (a) survey, (b) O 1s, (c) Cd 3d, and (d) Pb 4f.

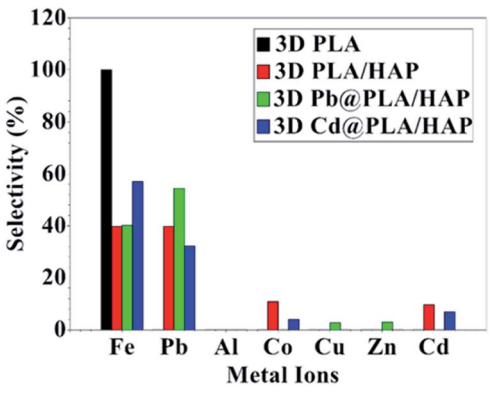

Fig. 6 The selectivity of the 3D printed objects towards the adsorption of metal ions. The selectivity is calculated based on the amount adsorbed in the metal ions divided by total amount of the adsorbed metal ions.

and Cd@PLA/HAp were tested to investigate the replacement of the adsorbed metal ions with the metal ions in the solution (Fig. 6).

The data analysis showing that 3D printing of pure PLA adsorbs mainly Fe^{3+} ions without significant adsorption of other metal ions (Fig. 6). PLA/HAp shows equal selectivity (39.7%) toward Fe^{3+} and Pb^{2+} ions with minimal selectivity (10%) toward Cd^{2+} and Co^{2+} without any observable adsorption toward metal ions such as Cu^{2+}, Zn^{2+}, and Al^{3+} (Fig. 6).

The adsorption affinity towards Fe^{3+} ions using PLA/HAp is mainly due to PLA (Fig. 6). This can be confirmed from the high adsorption selectivity (54.3%) of Pb^{2+} ions on PLA/HAp (Fig. 6). The selectivity toward Pb^{2+} over Cd^{2+} ions is mainly due to the difference in adsorption mechanisms, as mentioned above.

A comparison of the adsorption performance of PLA/HAp and HAp-based adsorbents with earlier reports is tabulated in Table 1. HAp was used as powder, foam, and hydrogels. A foam consist of poly(lactic acid)/hydroxyapatite (PLA/HAp) was fabricated using a supercritical CO_2.[10] The maximum adsorption capacity of Pb ions using PLA/HAp foam was increased from 81.2 mg g^{-1} to 140.5 mg g^{-1} with increasing the HAp content from 10 wt% to 40 wt%.[10] 3D printed filter in the current study contains only 15 wt% of HAp but showed higher adsorption capacity for Pb, in comparison (Table 1). The performance of our 3D printed filters were lower than some reports on HAp powder[70] or hydroxyapatite-impregnated magnetite–bentonite[71] which offers the possibility to magnetically separate the adsorbent after use. The high adsorption performance of hydroxyapatite-impregnated magnetite–bentonite was attributed to the functional groups of –OH–, $-PO_4^{3-}$ and $-NH_2$ on the surface.[71] The Table 1 also shows that PLA is a suitable matrix for the adsorption of Pb compared to other matrices such as polyacrylamide[21] and polyurethane[22] (Table 1). The presence of functional groups such as C=O and O–H in PLA also contributes to the adsorption performance. In general 3D printed PLA/HAp in the current study showed low adsorption capacity for Pb but high adsorption capacity for Cd (Table 1).

3D printed PLA/HAp filters show relevant adsorption performance and have the advantage that it can be easily separated from the aqueous solution without the need for magnetic nanoparticles or external magnet field, as in the case of Fe_3O_4/HAp (Table 1).[24]

4. Conclusions

PLA/HAp biocomposite was successfully prepared *via* solvent-assisted blending and thermally induced phase separation (TIPS) route and processed into highly-permeable 3D biofilters by FDM. SEM and μCT results showed a homogenous distribution of HAp in the matrix, channel interconnectivity and the consistent pore size and pore geometry over the entire filter structure, which indicate the applicability of this process route for developing 3D structured monoliths with controlled architecture. The high adsorption performance of the PLA/HAp composite towards heavy metal ions such as Pb^{2+} and Cd^{2+} was observed and was attributed to the synergistic effect of HAp and PLA. Water treatment using 3D printed PLA/HAp monolithic filters is therefore promising in terms of maximum adsorption capacity, high water flux without application of pressure, simple separation method after the adsorption process and its potential applicability to industrial processes. The biobased origin of the components and the scalability of the developed process route is expected to further contribute to sustainable and cost-effective water treatment. The recyclability of the PLA/HAp 3D printed filters and their end-of-life expectancy will be investigated in the future. The biological origin of the filter's components makes it a good candidate for biodegradation and recycling under controlled conditions and the heavy metal ions are expected to be desorbed from the filter structure with the means of chemical reaction (acid treatment), collected and potentially re-used within industrial applications. The designed 3D structures may be further exploited within the biomedical field, especially as bone regeneration scaffolds.

Author contributions

NF developed and 3D printed the biocomposite system and performed SEM, TGA, PXRD, FT-IR, EDS and water flux

Table 1 A summary for the adsorption of Pb^{2+} and Cd^{2+} using HAp based materials

Adsorbent	Form	Processing	HAp (%)	Adsorbate	Adsorption capacity (mg g^{-1})	Ref.
PLA/HAp	Foams	Supercritical CO_2 foaming	40	Pb	140.5	10
HAp	Powder	Hydrothermal	100	Cd	89.9	58
				Pb	154	
		Commercial synthetic HA		Cd	188.9	9
		Neutralization of $Ca(OH)_2$ with H_3PO_4, at room temperature		Cd	67.55	70
				Pb	676.09	
HAp/polyurethane	Foam	Immobilization	50	Pb	150	22
HAp/polyacrylamide	Hydrogel	Free radical polymerization	70	Pb	178	21
Fe_3O_4/HAp	Powder	Hydrothermal	85	Cd	219.9	24
		In situ precipitation	50	Pb	598.8	23
Fe_3O_4/HAp/bentonite		• Co-precipitation		Cd	309	71
		• Hydrothermal		Pb	482	
PLA/HAp	3D filter	3D printing	15	Cd	360.5	This study
				Pb	112.6	

measurements. HNA performed the heavy metal adsorption and XPS measurements. SAH performed the μCT measurements. BP and NT extracted and supplied the HAp from fish scale for the study. APM was in charge of the conceptualization and supervision of the project.

Conflicts of interest

There are no conflicts of interest to declare.

Acknowledgements

This work was funded by Knut and Alice Wallenberg Foundation (Wallenberg Wood Science Center) and the Swedish Foundation for Strategic Environmental Research (Mistra), project MISTRA TerraClean (project no. 2015/31). The authors wish to thank Anumol Ashok for her help with the TEM and Add North 3D AB, Ölsremma, Sweden for their help with the filament extrusion. The μ-CT imaging was performed at the 4D Imaging Lab at Lund University through financial support from Treesearch.

References

1 *The United Nations World Water Development Report 2020: Water and Climate Change – UNESCO Digital Library*, https://unesdoc.unesco.org/ark:/48223/pf0000372985.locale=en, accessed March 30, 2021.
2 L. Esrafili, F. D. Firuzabadi, A. Morsali and M.-L. Hu, *J. Hazard. Mater.*, 2021, **403**, 123696.
3 F. Yu, X. Bai, M. Liang and J. Ma, *Chem. Eng. J.*, 2021, **405**, 126960.
4 A. F. Abdel-Magied, H. N. Abdelhamid, R. M. Ashour, X. Zou and K. Forsberg, *Microporous Mesoporous Mater.*, 2019, **278**, 175–184.
5 R. M. Ashour, H. N. Abdelhamid, A. F. Abdel-Magied, A. A. Abdel-Khalek, M. M. Ali, A. Uheida, M. Muhammed, X. Zou and J. Dutta, *Solvent Extr. Ion Exch.*, 2017, **35**, 91–103.
6 D. Georgouvelas, H. N. Abdelhamid, J. Li, U. Edlund and A. P. Mathew, *Carbohydr. Polym.*, 2021, **264**, 118044.
7 H. Nasser Abdelhamid and A. P. Mathew, *Chem. Eng. J.*, 2021, **426**, 131733.
8 P. Liu, H. Sehaqui, P. Tingaut, A. Wichser, K. Oksman and A. P. Mathew, *Cellulose*, 2014, **21**, 449–461.
9 A. Corami, S. Mignardi and V. Ferrini, *J. Colloid Interface Sci.*, 2008, **317**, 402–408.
10 B. J. Jeon, Y. G. Jeong, B. G. Min, W. S. Lyoo and S. C. Lee, *Polym. Compos.*, 2011, **32**, 1408–1415.
11 K. Ioku, *J. Ceram. Soc. Jpn.*, 2010, **118**, 775–783.
12 S. Mondal, U. Pal and A. Dey, *Ceram. Int.*, 2016, **42**, 18338–18346.
13 E. Nejati, H. Mirzadeh and M. Zandi, *Composites, Part A*, 2008, **39**, 1589–1596.
14 L. J. Cummings, M. A. Snyder and K. Brisack, in *Methods in Enzymology*, ed. R. R. Burgess and M. P. Deutscher, Academic Press, 2009, vol. 463, pp. 387–404.
15 W. Condit, E. Hawley, H. Rectanus and R. Deeb, *J. Environ. Manage.*, 2017, **204**, 705–708.
16 M. Ibrahim, M. Labaki, J.-M. Giraudon and J.-F. Lamonier, *J. Hazard. Mater.*, 2020, **383**, 121139.
17 S. Mondal, S. Mahata, S. Kundu and B. Mondal, *Adv. Appl. Ceram.*, 2010, **109**, 234–239.
18 M. Boutinguiza, J. Pou, R. Comesaña, F. Lusquiños, A. de Carlos and B. León, *Mater. Sci. Eng. C*, 2012, **32**, 478–486.
19 Y.-C. Huang, P.-C. Hsiao and H.-J. Chai, *Ceram. Int.*, 2011, **37**, 1825–1831.
20 F. N. Oktar, S. Agathopoulos, L. S. Ozyegin, O. Gunduz, N. Demirkol, Y. Bozkurt and S. Salman, *J. Mater. Sci. Mater. Med.*, 2007, **18**, 2137–2143.
21 S. H. Jang, Y. G. Jeong, B. G. Min, W. S. Lyoo and S. C. Lee, *J. Hazard. Mater.*, 2008, **159**, 294–299.
22 S. H. Jang, B. G. Min, Y. G. Jeong, W. S. Lyoo and S. C. Lee, *J. Hazard. Mater.*, 2008, **152**, 1285–1292.
23 L. Dong, Z. Zhu, Y. Qiu and J. Zhao, *Chem. Eng. J.*, 2010, **165**, 827–834.
24 Y. Feng, J.-L. Gong, G.-M. Zeng, Q.-Y. Niu, H.-Y. Zhang, C.-G. Niu, J.-H. Deng and M. Yan, *Chem. Eng. J.*, 2010, **162**, 487–494.
25 Y. Wang, L. Hu, G. Zhang, T. Yan, L. Yan, Q. Wei and B. Du, *J. Colloid Interface Sci.*, 2017, **494**, 380–388.
26 C. Yan, S. Ma, Z. Ji, Y. Guo, Z. Liu, X. Zhang and X. Wang, *Polymers*, 2019, **11**, 774.
27 R. Xing, B. Yang, R. Huang, W. Qi, R. Su, B. P. Binks and Z. He, *Langmuir*, 2019, **35**, 12799–12806.
28 Z. Shi, C. Xu, F. Chen, Y. Wang, L. Li, Q. Meng and R. Zhang, *RSC Adv.*, 2017, **7**, 49947–49952.
29 K. Kim, M. C. Ratri, G. Choe, M. Nam, D. Cho and K. Shin, *PLoS One*, 2020, **15**, e0231475.
30 L. A. Lagalante, A. J. Lagalante and A. F. Lagalante, *J. Water Process. Eng.*, 2020, **35**, 101194.
31 Y. S. Nam and T. G. Park, *Biomaterials*, 1999, **20**, 1783–1790.
32 J. J. Blaker, J. C. Knowles and R. M. Day, *Acta Biomater.*, 2008, **4**, 264–272.
33 G. Wei and P. X. Ma, *Biomaterials*, 2004, **25**, 4749–4757.
34 G. Radha, S. Balakumar, B. Venkatesan and E. Vellaichamy, *Mater. Sci. Eng. C*, 2017, **75**, 221–228.
35 V. Mazzanti, L. Malagutti and F. Mollica, *Polymers*, 2019, **11**, 1094.
36 A. A. Vaidya, C. Collet, M. Gaugler and G. Lloyd-Jones, *Mater. Today Commun.*, 2019, **19**, 286–296.
37 X. Wang, M. Jiang, Z. Zhou, J. Gou and D. Hui, *Composites, Part B*, 2017, **110**, 442–458.
38 M. A. Sawpan, K. L. Pickering and A. Fernyhough, *Composites, Part A*, 2011, **42**, 1189–1196.
39 M. Kowalczyk, E. Piorkowska, P. Kulpinski and M. Pracella, *Composites, Part A*, 2011, **42**, 1509–1514.
40 K. Okubo, T. Fujii and E. T. Thostenson, *Composites, Part A*, 2009, **40**, 469–475.
41 Y. Tao, H. Wang, Z. Li, P. Li and S. Q. Shi, *Materials*, 2017, **10**, 339.
42 Z. Wang, J. Xu, Y. Lu, L. Hu, Y. Fan, J. Ma and X. Zhou, *Ind. Crops Prod.*, 2017, **109**, 889–896.

43 X. Tian, T. Liu, C. Yang, Q. Wang and D. Li, *Composites, Part A*, 2016, **88**, 198–205.
44 M. Heidari-Rarani, M. Rafiee-Afarani and A. M. Zahedi, *Composites, Part B*, 2019, **175**, 107147.
45 C. E. Corcione, F. Gervaso, F. Scalera, F. Montagna, T. Maiullaro, A. Sannino and A. Maffezzoli, *J. Polym. Eng.*, 2017, **37**, 741–746.
46 C. Esposito Corcione, F. Gervaso, F. Scalera, S. K. Padmanabhan, M. Madaghiele, F. Montagna, A. Sannino, A. Licciulli and A. Maffezzoli, *Ceram. Int.*, 2019, **45**, 2803–2810.
47 H. Zhang, X. Mao, Z. Du, W. Jiang, X. Han, D. Zhao, D. Han and Q. Li, *Sci. Technol. Adv. Mater.*, 2016, **17**, 136–148.
48 R. N. Zare, E. Doustkhah and M. H. N. Assadi, *Mater. Today: Proc.*, 2021, **42**(part 3), 1531–1533.
49 J. Ferri, J. Jordá, N. Montanes, O. Fenollar and R. Balart, *J. Thermoplast. Compos. Mater.*, 2018, **31**, 865–881.
50 F. S. Senatov, K. V. Niaza, M. Yu. Zadorozhnyy, A. V. Maksimkin, S. D. Kaloshkin and Y. Z. Estrin, *J. Mech. Behav. Biomed. Mater.*, 2016, **57**, 139–148.
51 G. Conoscenti, V. L. Carrubba and V. Brucato, *Arch. Chem. Res.*, 2017, **1**(2), 12, ISSN 2572-4657.
52 F.-D. Kopinke, M. Remmler, K. Mackenzie, M. Möder and O. Wachsen, *Polym. Degrad. Stab.*, 1996, **53**, 329–342.
53 C. J. Liao, F. H. Lin, K. S. Chen and J. S. Sun, *Biomaterials*, 1999, **20**, 1807–1813.
54 N. Pleshko, A. Boskey and R. Mendelsohn, *Biophys. J.*, 1991, **60**, 786–793.
55 H. Montazerian, M. G. A. Mohamed, M. M. Montazeri, S. Kheiri, A. S. Milani, K. Kim and M. Hoorfar, *Acta Biomater.*, 2019, **96**, 149–160.
56 B. Pasha Mahammod, E. Barua, A. B. Deoghare and K. M. Pandey, *Mater. Today: Proc.*, 2020, **22**, 1687–1693.
57 J. C. Igwe and A. A. Abia, *Ecletica Quim.*, 2007, **32**, 33–42.
58 S. Lazarević, I. Janković-Častvan, D. Tanasković, V. Pavićević, D. Janaćković and R. Petrović, *J. Environ. Eng.*, 2008, **134**, 683–688.
59 N. C. C. da Rocha, R. C. de Campos, A. M. Rossi, E. L. Moreira, A. do F. Barbosa and G. T. Moure, *Environ. Sci. Technol.*, 2002, **36**, 1630–1635.
60 J. A. Gómez del Río, P. J. Morando and D. S. Cicerone, *J. Environ. Manage.*, 2004, **71**, 169–177.
61 J. Gómez del Río, P. Sanchez, P. J. Morando and D. S. Cicerone, *Chemosphere*, 2006, **64**, 1015–1020.
62 A. Ramdani, A. Kadeche, M. Adjdir, Z. Taleb, D. Ikhou, S. Taleb and A. Deratani, *Water Pract. Technol.*, 2020, **15**, 130–141.
63 Md R. Awual, *J. Environ. Chem. Eng.*, 2019, **7**, 103378.
64 H. R. Mortaheb, H. Kosuge, B. Mokhtarani, M. H. Amini and H. R. Banihashemi, *J. Hazard. Mater.*, 2009, **165**, 630–636.
65 J. Acharya, J. N. Sahu, C. R. Mohanty and B. C. Meikap, *Chem. Eng. J.*, 2009, **149**, 249–262.
66 Md R. Awual, *J. Environ. Chem. Eng.*, 2019, **7**, 103087.
67 J. Vodela, J. Renden, S. Lenz, W. McElhenney and B. Kemppainen, *Poult. Sci.*, 1997, **76**, 1474–1492.
68 P. J. Harvey, H. K. Handley and M. P. Taylor, *Environ. Res.*, 2016, **151**, 275–285.
69 M. A. M. Mohamed, M. A. Osman, T. L. Potter and R. E. Levin, *Environ. Int.*, 1998, **24**, 767–772.
70 I. Smičiklas, A. Onjia, S. Raičević, Đ. Janaćković and M. Mitrić, *J. Hazard. Mater.*, 2008, **152**, 876–884.
71 Q. U. Ain, H. Zhang, M. Yaseen, U. Rasheed, K. Liu, S. Subhan and Z. Tong, *J. Cleaner Prod.*, 2020, **247**, 119088.